Experimental Determination of the Conditions Associated with "Zebra Stripe" Pattern Generation in the Earth's Inner Radiation Belt

Solène Lejosne[1], F.S. Mozer[1]

1. Space Science Laboratory, University of California, Berkeley

Corresponding author: S. Lejosne, solene@berkeley.edu

Key words

Zebra Stripes – Superposed Epoch Analysis – Prompt Penetration Electric Fields – Inner Radiation Belt – Substorm

Key Points

1. An algorithm is designed to analyze the zebra stripes present in the spectrograms of energetic electrons trapped in the inner belt.

2. A superposed epoch analysis of 370 events is performed to determine the experimental conditions associated with zebra stripe generation.

3. Experimental evidence suggests that prompt penetration electric fields associated with substorm onsets routinely generate zebra stripes.

Abstract

The "zebra stripes" are peaks and valleys commonly present in the spectrograms of energetic particles trapped in the Earth's inner belt. Several theories have been proposed over the years to explain their generation, structure and evolution. Yet, the plausibility of various theories has not been tested due to a historical lack of ground-truth, including in-situ electric field measurements. In this work, we leverage the new visibility offered by the database of NASA Van Allen Probes electric drift measurements to reveal the conditions associated with the generation of zebra stripe patterns. Energetic electron flux measurements by the Radiation Belt Storm Probes Ion Composition Experiment between January 1, 2013 and December 31, 2015 are systematically analyzed to determine 370 start times associated with the generation of zebra stripes. Statistical analyses of these events reveal that the zebra stripes are usually created during substorm onset, a time at which prompt penetration electric fields are present in the plasmasphere. All the pieces of experimental evidence collected are consistent with a scenario in which the prompt penetration electric field associated with substorm onset leads to a sudden perturbation of the trapped particle drift motion. Subsequent inner belt drift echoes constitute the zebra stripes. This study exemplifies how the analysis of trapped particle dynamics in the inner belt and slot region provides complimentary information on the dynamics of plasmaspheric electric fields. It is the first time that the signature of prompt penetration electric fields is detected in near-equatorial electric field measurements below L=3.

1. Introduction

Spectrograms of energetic (tens to hundreds of keV) particles trapped in the Earth's inner radiation belt commonly display time-varying structured peaks and valleys (Imhof and Smith, 1965; Imhof et al., 1981a, 1981b; Datlowe et al., 1985; Sauvaud et al., 2013). These features have been recently named the "zebra stripes" (Ukhorskiy et al., 2014). Newly found "Earth-like zebra stripes" have also been reported in the electron radiation belt of Saturn (Sun et al., 2019).

One characteristic of the terrestrial zebra stripes is that every peak, and similarly, every valley, corresponds to a population of trapped particles with similar magnetic drift frequencies (Sauvaud et al., 2013). As a result, the zebra stripes are usually straight lines when the measured fluxes are represented in the (L, drift frequency) space. However, the zebra stripe pattern can appear disturbed during times of enhanced magnetic activity (Ukhorskiy et al., 2014). Another feature of the zebra stripes is that they seem to tighten and narrow when observed during consecutive passes: The drift frequency separation between successive peaks (and valleys) decreases linearly with time (Lejosne & Roederer, 2016; Liu et al., 2016). In that context, the structure of the zebra stripes is comparable a stopwatch in that the drift frequency separation between successive peaks and valleys contains temporal information. This temporal information corresponds to the time spent by the particles drifting since some initial "reset" time or "start time" (e.g., Lejosne & Roederer, 2016). What this start time represents has never been examined so far.

Several theories have been proposed over the years in order to explain the generation, structure and evolution of the zebra stripe pattern in the Earth's inner belt (e.g., Cladis, 1966; Pinto et al., 1991; Sauvaud et al., 2013; Ukhorskiy et al., 2014; Lejosne & Roederer, 2016; Selesnick et al., 2016; Liu et al., 2016). While most theories involve an ad-hoc electric model, it has not been possible to test their plausibility because of a historical lack of ground-truth (e.g. Su et al., 2016). Providing reliable electric field measurements near the magnetic equator in the plasmasphere is indeed a technical challenge (e.g., Lejosne & Mozer, 2016a, 2016b; Mozer, 2016). As a result, it has been unclear how zebra stripes are generated in the Earth's inner belt.

The instruments onboard the Van Allen Probes were the first instruments to provide reliable evaluation of the near-equatorial electric drift $\mathbf{E} \times \mathbf{B}/\mathrm{B}^2$ in the Earth's plasmasphere (e.g., Lejosne & Mozer, 2016a, 2016b, Lejosne et al., 2017, Lejosne & Mozer, 2018, 2019). For this work, we have leveraged the new visibility offered by Van Allen Probes electric drift measurements to determine experimentally the processes associated with the generation of zebra stripe patterns. The approach is as follows: First, we examine three years of electron flux measurements to detect zebra stripe patterns in the Earth's inner belt. We use these observations to establish a list of 370 start times associated with the generation of zebra stripes. The method developed for establishing the list of zebra stripe generation events is detailed in the **Section 2**. Then, we conduct a superposed epoch analysis to provide information on (**Section 3.1**) the zebra stripe lifetime, (**Section 3.2**) the magnetic activity associated zebra stripe generation, (**Section 3.3**) the initial azimuthal locations for the populations corresponding to the peaks and valleys in the zebra stripes, and (**Section 3.4**) the electric field dynamics during zebra stripe generation.

Statistical analyses reveal that the zebra stripe generation is usually associated with substorm onset and the emergence of prompt penetration electric fields. It also shows that the peaks in the zebra stripes usually correspond to trapped particles present in the morning region at start time, while the valleys in the stripes usually correspond to particles present in the dusk-premidnight region at start time. All the gathered pieces of experimental information are consistent with a scenario in which the zebra stripes usually result from the action of magnetospheric convection penetrating the plasmasphere during substorm onset.

2. Data and Methodology

2.1. Data: Field and Particle Measurements by the NASA Van Allen Probes

The study relies Van Allen Probes field and particle measurements between January 1, 2013 and December 31, 2015. This time interval corresponds to the prime phase of the mission, i.e., a time during which the best quality measurements were recorded in a sufficient number to perform a statistical analysis. The two Van Allen Probes RBSP A and RBSP B had an apogee at 5.8 Earth

radii, a perigee around 1,000 km, a period of 9 hr and an inclination of 10°. The spacecraft orbits drifted slowly so that it took little less than two years for spacecraft apogees to scan all local time sectors.

For the field measurements, we preprocessed the spin-averaged (12 s) electric (Wygant et al., 2013) and magnetic (Kletzing et al., 2013) field measurements to derive reliable evaluations of the electric drift in a frame of reference fixed to the stars. The preprocessing consists of three steps: (1) A slight misalignment in the magnetometer axes for both spacecraft is corrected (Lejosne & Mozer, 2016a, 2016b). (2) The data from the less reliable short-axis electric field antenna is replaced by the assumption that the parallel electric field is zero, because of the plasma's high conductivity parallel to magnetic field lines. (3) The shorting factor is set to a value close to 1, leading to margins of errors of a few m/s (Lejosne & Mozer, 2019). The electric drift measurements are then projected to the magnetic equator, assuming equipotential field lines and a realistic magnetic field model (Lejosne & Mozer, 2016b).

For the particle measurements, we focus on the level 3 Pitch Angle and Pressure data by the Radiation Belt Storm Probes Ion Composition Experiment (RBSPICE) (Mitchell et al., 2013). The high energy resolution, low time resolution, electron species rates (ESRHELT) product provides unidirectional differential electron fluxes for 17 pitch angle channels and 64 energy channels. The pitch angle channels have a resolution of 10 degrees – expect in the first and last bins, where the resolution is15 degrees. The energy channels are logarithmically spaced and they cover the [20 keV-938 MeV] energy range.

2.2. Methodology: "Zebra Stripe" Pattern Detection and Analysis

Because the zebra stripes are approximate straight lines when the fluxes are represented in the (L, drift frequency) space, we first describe how information on particle energy, pitch angle and spacecraft location is converted into information on magnetic drift frequency (**Section 2.2.1**). Then, we present the algorithm designed to detect and analyze the zebra stripes observed by the RBSPICE instrument in the **Section 2.2.2**. In the **Section 2.2.3.**, we explain how the results are compiled to establish the list of 370 start times associated with zebra stripe generation.

142

143 *2.2.1. Determining the drift frequency associated with each RBSPICE data point*

144 Information on kinetic energy, T, pitch angle, α, and spacecraft location, L, is converted into
145 information on trapped electron magnetic drift frequency, $\Omega/2\pi$, applying Schulz and Lanzerotti's
146 formulas (1974) in the case of a dipole magnetic field:

147

$$\Omega = \frac{3L}{qB_E R_E^2} \frac{T(T+2E_0)}{T+E_0} \frac{D(y_0)}{T(y_0)} \quad (1)$$

148

149 where $E_0 = 0.511\ MeV$ is the electron rest mass energy, y_0 is the sine of the equatorial pitch angle,
150 $B_E = 30{,}000\ nT$ is the equatorial magnetic field at the surface of the Earth, $R_E = 6{,}371.2\ km$ is
151 one Earth radius, and D and T are the following pitch-angle functions:

152

$$D(y_0) = \frac{5.520692 - 2.357194 \times y_0 + 1.279385 \times y_0^{3/4}}{12} \quad (2)$$

153 and

154

$$T(y_0) = 1.380173 - 0.639693 \times y_0^{3/4} \quad (3)$$

155

156 Because there can be up to 20 degrees between the spacecraft location and the magnetic equator
157 the value of the equatorial pitch angle is obtained from the value of the local pitch angle, $\alpha =$
158 $\sin^{-1} y$:

159

$$y_0 = y\sqrt{\frac{B_0}{B}} \quad (4)$$

160

161 where B is the local magnetic field magnitude, and B_0 is the magnetic field magnitude at the
162 magnetic equator following the field line passing through spacecraft location at the time of
163 measurement. The coefficients $\sqrt{B_0/B}$ are computed using the Fortran Library International

Radiation Belt Environment Modeling IRBEM-LIB (Boscher et al., 2012) assuming that the magnetic field is well described by the International Geomagnetic Reference Field model (IGRF) below L = 3.

2.2.2. Creating and analyzing the unidirectional spectra measured during each inner belt pass

We divide the three year interval of RBSPICE data into approximately 6,000 inbound or outbound passes per spacecraft below L = 3. This results into the creation of approximately 12,000 three-dimensional matrices in which the electron flux is provided as a function of (1) kinetic energy, (2) pitch angle, and (3) time (or, equivalently, spacecraft location). Given the amount of data involved, an algorithm has been developed to analyze all the spectrograms. The objective of the algorithm is to detect and describe the structure of the zebra stripes when present. The different criteria set for zebra stripe detection and analysis are documented in the following. The algorithm is made of four steps. Three consecutive steps are applied to every pass, every pitch angle channel, and every sampling time. The information resulting from these three steps is then compiled and analyzed in a fourth step.

Step 1: Detrending the fluxes

First, we define a smoothed flux following the approach presented by Liu et al. (2016). For each energy channel, the value of the logarithm of the smoothed flux is equal to the running average of the logarithms of the measured fluxes over nine consecutive energy bins (+/- four energy bins around the energy channel considered). The logarithm of the flux is then detrended by subtracting the logarithm of the smoothed flux to the measured logarithmic flux. An illustration for this step is provided **Figure 1**.

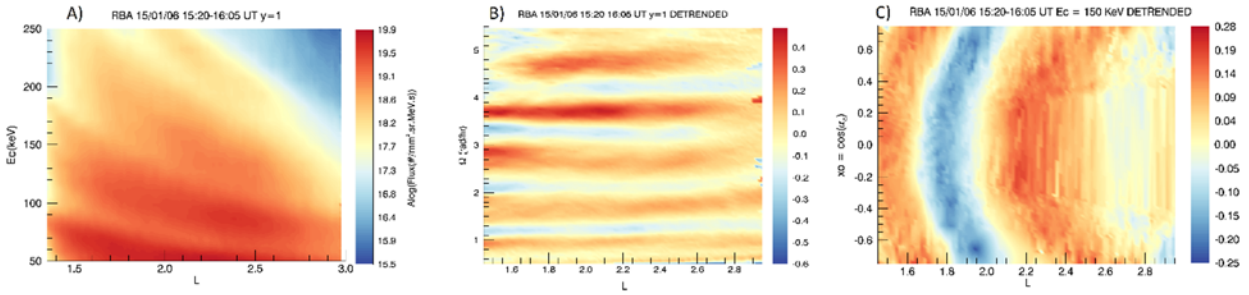

Figure 1. Detrending the unidirectional differential electron fluxes measured by Van Allen Probe A (RBA) during an inner belt pass in January 6, 2015 (15:20 UT – 16:05 UT). The Panel A)

corresponds to the 90° pitch angle channel ($y = 1$), and it displays the flux as a function of kinetic energy, E_c, and spacecraft location, L. B) The same spectrum as the one displayed Panel A), but detrended. The logarithm of the detrended flux is represented as a function of spacecraft location, L, and magnetic angular drift velocity, Ω. C) The logarithm of the detrended flux for 150 keV electrons, represented as a function of spacecraft location, L, and equatorial pitch angle $x_o = \cos\alpha_o$. The peaks and valleys are more apparent Panels B) and C) than Panel A). They correspond to populations of particles with similar magnetic drift frequencies.

The **Figure 1A** shows that the zebra stripe pattern was present in the inner belt on January 6, 2015, between 15:20 UT and 16:05 UT. Detrending the fluxes emphasizes the zebra stripe patterns (**Figure 1B-C**). The zebra stripes correspond to approximate straight lines when represented in the (L, Ω) space at constant equatorial pitch angle, α_o, as illustrated **Figure 1B**. They correspond to curved lines when represented in the $(L, \cos\alpha_o)$ space, as illustrated **Figure 1C**. Both features are consistent with the fact that every structured peak and valley corresponds to a population of particles with similar magnetic drift frequencies, $\Omega/2\pi$, as described by the **equation (1)**.

Step 2: Extracting the spectrum peaks and valleys

For every pitch angle channel, we compute the derivative of the logarithm of the detrended spectrum with respect to the logarithm of the magnetic drift frequency. A local extremum in the detrended flux (minimum or maximum) corresponds a magnetic drift frequency at which the derivative is changing sign. We also compute the second derivative in order to determine whether a local extremum corresponds to a local minimum or a local maximum in the detrended flux. In addition, the value of the detrended flux at every extremum is stored in order to quantify the magnitude of the stripes. Because the objective of the algorithm is to focus on clear zebra stripe patterns in the tens to hundreds of keV energy range, we filter the resulting data points according to two selection criteria. We discard extrema corresponding to (1) high energy channels ($\Omega \geq \sim 1$mHz, thus $\geq \sim 1MeV$) and (2) faint stripes (when the difference between the flux and the smooth flux is smaller than 5% on average).

Step 3: Converting the peak and valley information into time information

Following the theory proposed by Lejosne and Roederer (2016), we consider that the central energies of consecutive peaks and valleys correspond to those electrons that have swept the same angular portions $\Delta\varphi$ modulo 2π since some unspecified start time, t_0, from some unspecified initial angular location $\varphi(t_0)$. An illustration is provided **Figure 2**.

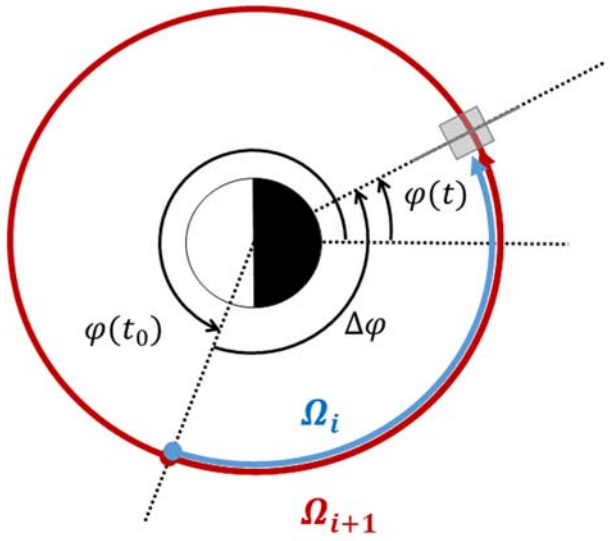

Figure 2. The central energies of consecutive peaks and valleys correspond to those electrons which have swept the same angular portions $\Delta\varphi$ modulo 2π since some undefined start time t_0, and from undefined initial angular location $\varphi(t_0)$. The spacecraft is represented by a grey square, and its azimuthal location at the time of measurement t is $\varphi(t)$. Two angular drift velocities indicative of two consecutive local minima (or two consecutive local maxima) in the detrended flux are Ω_i and Ω_{i+1}. They both correspond to populations of particles located at $\varphi(t_0)$ at the start time t_0, and detected by the spacecraft instruments at time t. Thus, both populations are also located at $\varphi(t)$ at time t. The population with angular drift velocity Ω_{i+1} has traveled $\Delta\varphi + 2\pi$ during the time interval $\Delta T = t - t_0$ while the population with angular drift velocity Ω_i has traveled $\Delta\varphi$ during the same time interval ΔT.

With Ω_i and Ω_{i+1} two angular drift velocities indicative of consecutive local minima (or consecutive local maxima) in the detrended flux:

$$\Omega_{i+1}(t - t_0) = \Omega_i(t - t_0) + 2\pi \quad (5)$$

Thus:

$$\Delta T_i = \frac{2\pi}{\Delta\Omega_i} \quad (6)$$

where ΔT_i indicates the time spent since a potential start time, t_0, according to the separation between two consecutive peaks or valleys present in a spectrum measured at time, t, $\Delta\Omega_i = |\Omega_{i+1} - \Omega_i|$. For both series of local minima and local maxima defined **Step 2**, the sets of time intervals (ΔT_i) and associated start times $\left(t_{0,i} = t - \Delta T_i\right)$ are computed. If both theory and observations were perfect, all the processed time intervals, ΔT_i, would refer to the same initial start time, t_0, in the presence of zebra stripes. In practice, each pass produces a set of potential start times, $\left(t_{0,i}\right)$, that is more or less scattered. Thus, we further analyze this set in order to differentiate the information from the noise, and to determine the most likely start time, when defined.

Step 4: Analyzing the set of potential start times $\left(t_{0,i}\right)$

Once all the different pitch angle channels and sampling times are processed according to the **Steps 1-3**, the results are further analyzed to determine the most likely start time (when present). First, for each pass, all the potential start times, $\left(t_{0,i}\right)$, are compiled in a histogram with a bin size of one hour,. The points corresponding to the less populated bins are discarded ($n/N_{max} \leq 0.5$, with N_{max}, the maximum number of points per bin, and n, the number of points in the bin considered). Second, a Hough transform (e.g., Duda and Hart, 1972) is applied to each of the two sets of extrema (minima and maxima) in the (L, Ω) space in order to detect the presence of stripes. The Hough transform is a technique used in image processing in order to extract imperfect features. Data points that are not located along horizontal stripes (+/- 10 degrees) are discarded. This two-step sequence (histogram, Hough transform) is repeated until no additional data point is discarded. An illustration of this filtering method is provided **Figure 3**.

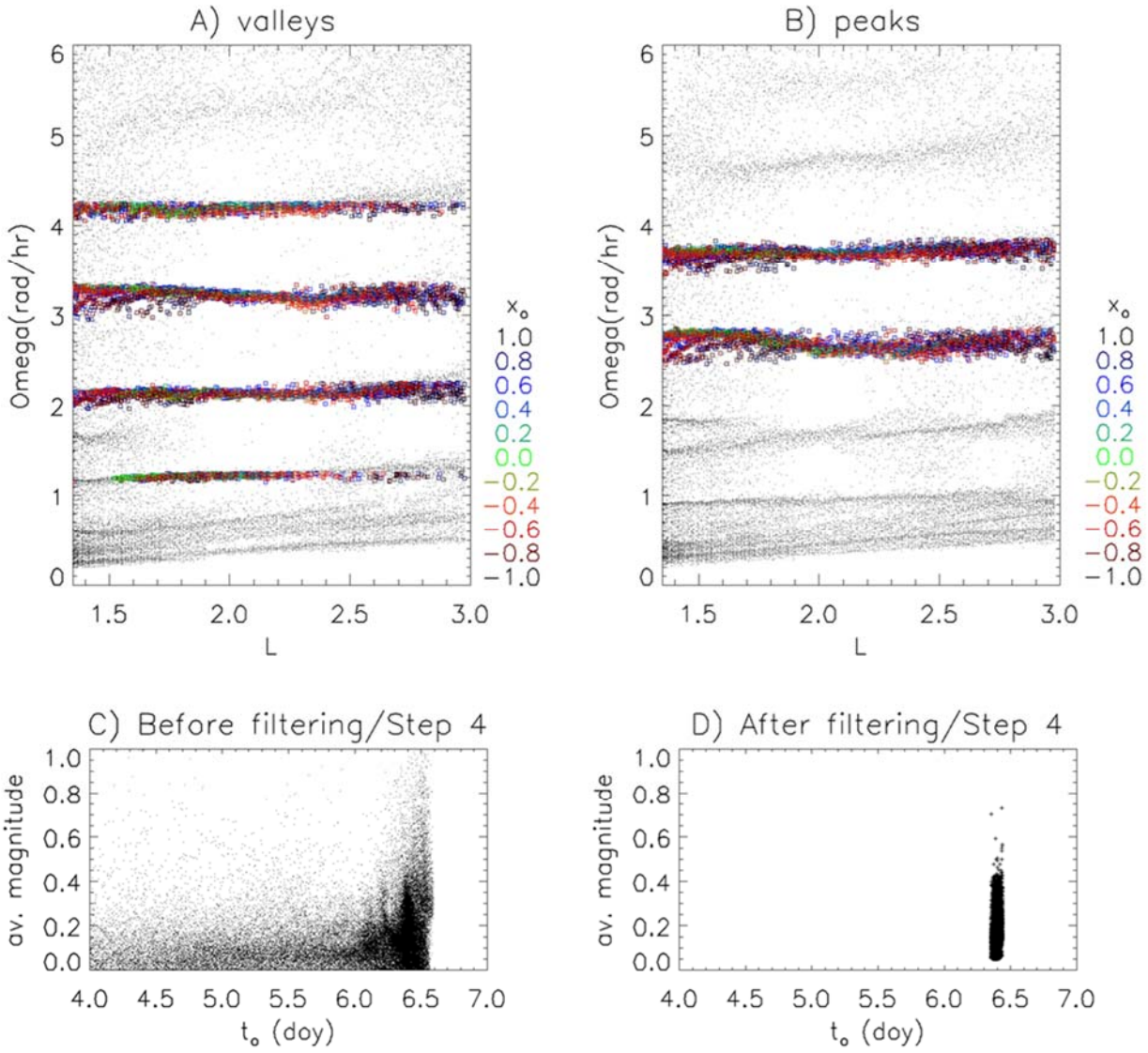

Figure 3. the (A) valleys and (B) peaks extracted from the analysis of the detrended flux, during the same pass as **Figure 1 (**January 6, 2015 15:20 UT – 16:05 UT). The data points resulting from the analysis of the detrended flux (**Step 2**) are represented by black dots. The data points selected after Hough transform and histogram analysis (**Step 4**) are displayed in a square whose color is related to the pitch angle channel considered ($x_o = \cos\alpha_o$). The set of potential start times, ($t_{0,i}$), is represented as a function of the average magnitude of the associated stripes in the Panels C) and D). The data points selected after Hough transform and histogram analysis are shown Panel D).

During the pass illustrated **Figure 1,** multiple peaks and valleys are found in the unidirectional differential electron fluxes. They correspond to the black dots displayed **Figure 3A** for the valleys and **Figure 3B** for the peaks. Both cloud plots display some stripes in the (L, Ω) space, together with some noise, especially at low ($\Omega \leq 0.5\, rad/hr$) and high ($\Omega \geq 5\, rad/hr$) energies. Depending on the pass, the stripes are more or less regular, and more or less continuous. They can even sometimes display a slight dependence on L (as illustrated for instance **Figure 3B** for $\Omega \sim 4.5\, rad/hr$). The **Step 4** of the algorithm is designed in an attempt to differentiate signal and noise. The data points selected after filtering are the color-coded squares **Figure 3**. The variety of colors represents the variety of equatorial pitch angles present in the selection. This shows that the filtering process captures most of the stripes while successfully excluding most of the noise from further analysis (**Figure 3C-D**). A limit to the procedure is that irregular stripes can also be discarded (e.g., $\Omega \sim 1.8\, rad/hr$ **Figure 3B**).

2.2.3. Determining a list of start time intervals associated with zebra stripe generation

The objective is to select a sufficient number of good (i.e., clear, strong) events to enable a statistical analysis of the conditions associated with zebra stripe generation. The approach chosen to determine a list of good events is detailed in the following.

All the potential start times, $(t_{0,i})$, resulting from the analysis described **Section 2.2.2** are stored, together with information on (1) the pass during which they are determined, (2) the couple of angular drift velocities used to estimate this potential start time, (Ω_i, Ω_{i+1}), and (3) the average magnitude of the associated flux fluctuation. We then use this information to create monthly histograms called "zebra stripe generation indicators". The histograms are defined as follows. The tables have a bin size of two hours, and each element corresponds to the number of points, $(t_{0,i})$, that refer to the two-hour time interval considered. The tables are then normalized by the monthly maximum per bin. The procedure is carried with and without weighting the number of points by the average magnitudes of the corresponding flux fluctuations. The resulting histograms can be interpreted as local quantifications for the likelihood of zebra stripe generation.

Since the objective is to find as many good events as possible while limiting the number of false positives, we define a set of three criteria that a selected event must verify in order to be listed as a "good" event. First, the start time selected must be in a bin that corresponds to a local maximum in the "zebra stripe generation indicators". Second, the start time selected must be apparent in at

least two different passes. Third, the average amplitude of the stripes associated with the process occurring at the start time selected must relatively large (more precisely, the average amplitude must be greater than 90% of the computed monthly max). For the three years of data considered, 370 events fulfilled this set of criteria.

An illustration is provided **Figure 4** in the case of the month of August 2013. The nine start times selected that month are also indicated. The histogram of "zebra stripe generation indicators" is represented **Figure 4D** together with different time series of magnetic activity indices, namely, the auroral electrojet index, AE (**Figure 4A**), the north-south component of the interplanetary magnetic field, IMF, B_z (**Figure 4B**), the polar cap potential, PCP, computed according to the formula by Boyle et al. (1997) (**Figure 4C**). Two different "zebra stripe generation indicators" are computed (with and without taking into account the magnitude of the resulting stripes). The **Figure 4** shows that both methods usually agree with each other, meaning that the most intense zebra stripe events usually generate the highest numbers of consistent information (i.e., the strongest events are also usually the cleanest).

The **Figure 4** suggests that favorable times to zebra stripe generation (i.e. large local maxima in the zebra stripe indicators) are usually associated with an increase in the auroral electroject, a decrease in the north-south component of the interplanetary magnetic field, and an increase in the polar cap potential. Thus, **Figure 4** suggests that there is a correlation between substorm onset and the mechanism leading to the generation of zebra stripes. The **Figure 4** also illustrates the limitations of the proposed method. Indeed, the filter seems to have missed an event occurring during the day of the year (doy) 225 and one or two events occurring during the doy 243 for instance.

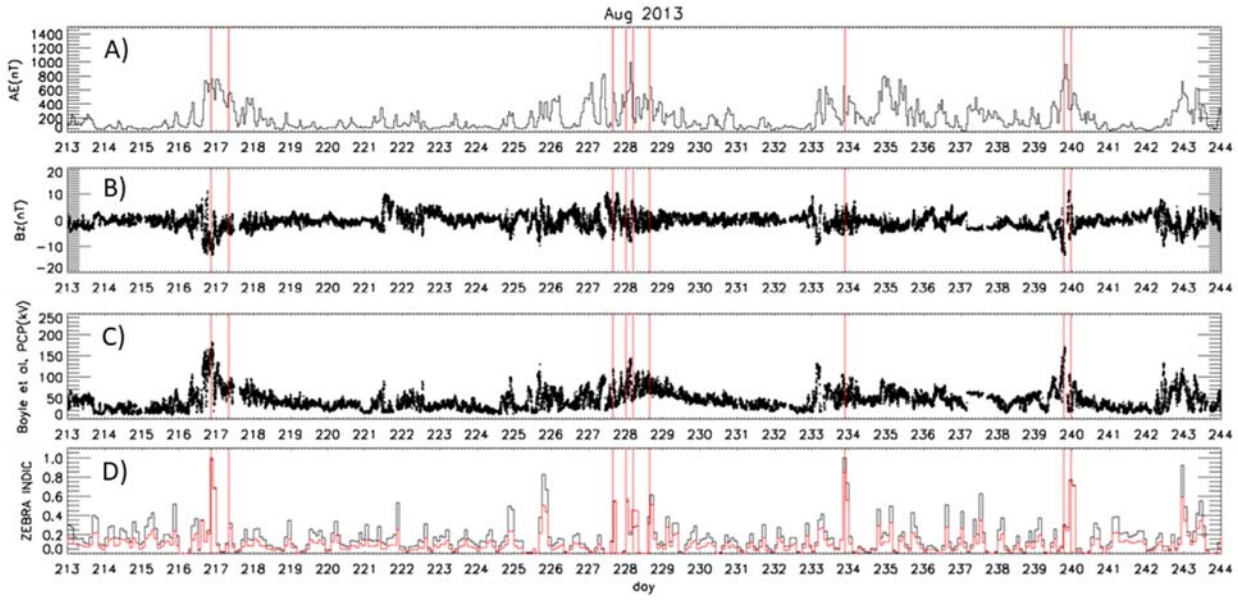

Figure 4. Magnetic activity indices and "zebra stripe generation indicators" (A) the auroral electrojet index, AE (B), the north-south component of the solar wind, B_z and (C) the polar cap potential, PCP, according to the formula by Boyle et al. (1997). Different "zebra stripe generation indicators" are computed with (in red) and without (in black) taking into account the magnitude of the resulting stripes. Vertical red lines indicate the nine start times selected in August 2013.

2.2.4. Determining the start time, t_0, and the margin of error associated with each zebra stripe generation event

For each of the 370 events, we compile all the corresponding information from the (> 2) associated passes. The mean start time, t_0, is defined as the average of all possible start times, and the margin of error is defined as the standard deviation of the set of possible start times $(t_{0,i})$: The average standard deviation obtained is of the order of an hour.

A second method to determine the most likely start time has also been tested. This method relies on the idea that all the particles with energies located at the center of peaks (or valleys) have swept the same angular portions $\Delta\varphi$ modulo 2π since the start time, t_0. Thus, given a data point corresponding to 1) a peak – or a valley (Ω_i), 2) a time and place of measurement $(t, \varphi(t))$, and 3) a potential start time t_0, the associated start time azimuthal location $\varphi(t_0)$ is:

$$\varphi(t_0) = \varphi(t) - (\Omega_i + \Omega_E)(t - t_0)\ [2\pi] \quad (7)$$

where $\Omega_i/2\pi$ is the magnetic drift frequency associated with the center of a peak (or a valley) and $\Omega_E/2\pi$ is the corotation frequency. If both data and theory were perfect, $\varphi(t_0)$ would not depend on the data point Ω_i considered (see also **Figure 2**). In practice, $\varphi(t_0)$ varies with Ω_i. Thus, the most likely start time can also be defined as the time t_0 which minimizes the scattering between all possible initial azimuthal locations, $\varphi(t_{0,i})$, computed according to the **equation (7)**. The most likely start time found with this method is usually located 20 min after the most likely start time found with the most straightforward method. Given that the standard deviation is of the order of an hour, both methods provide equivalent answers.

The list of the 370 start times associated with the zebra stripe pattern generation between January 1, 2013 and December 31, 2015 is accessible online (https://doi.org/10.5281/zenodo.3637636).

3. Experimental Determination of the Conditions Associated With Zebra Stripe Generation: a Statistical Analysis

3.1. Zebra Stripe Lifetime

Because zebra stripe patterns are often detected over consecutive passes (e.g. Fig.8 in Lejosne & Roederer, 2016), we first use the list of 370 zebra stripe generation events to estimate the lifetime of zebra stripe patterns. The typical start time for zebra stripe observations is defined as the average of the minimum time intervals detected per event, $\min(\Delta T_i)$. The typical stop time for zebra stripe observations is defined as the average of the maximum time intervals per event, $\max(\Delta T_i)$. The resulting typical start time for zebra stripe observations is 6.5 hours after t_o while the typical stop time for zebra stripe observations is 14.5 hours after t_o. Thus, zebra stripes are typically be observed during 8 hours, from 6.5 to 14.5 hours after t_o.

That the zebra stripes are not detected directly after triggering can be explained by considering the **equation (6)**. The smaller the time interval ΔT_i, the bigger the difference between Ω_i and Ω_{i+1}.

Thus, in order to observe some zebra stripes just after their generation, i.e., in order to detect stripes after a brief time interval, ΔT, one needs to analyze a particle spectrum over a very wide energy range. Yet, the amplitude of the stripes usually decreases with kinetic energy. (This is because the effect of a disturbance in the electric drift is less and less significant as the kinetic energy increases. This point will be further discussed **Section 3.3**). Thus, the zebra stripes are most apparent in the tens to hundreds of keV energy range. As a result, the zebra stripes are usually undetected immediately after generation. A time lag is required so that the distance between Ω_i and Ω_{i+1} decreases and at least two stripes become apparent. Similarly, as the time interval ΔT increases, the distance between Ω_i and Ω_{i+1} decreases until $\Omega_i \cong \Omega_{i+1}$. The stripes become too tight for the finite energy resolution of the instrument. They are then indiscernible. In addition, as time goes by, it becomes less and less likely that the zebra stripe pattern remains clear, as additional disturbances to the electric drift may occur. As a result, zebra stripes have a finite lifetime that we estimate to be of the order of half a day.

3.2. Magnetic Activity During Zebra Stripe Lifetime

The time series of different magnetic indices and solar wind parameters are stored for each of the 370 zebra stripe generation events. The time origin is set to the start time t_o. The time interval examined starts 4 hours before t_o and ends 17 hours after t_o. At each instance between $t_o - 4hr$ and $t_o + 17hr$, the cumulative distributions are examined and the distribution deciles are stored. The magnetic indices examined are the auroral electrojet (AE), the Kp index, the Dst index, and the polar cap potential (PCP) according to the formula Boyle et al. (1997). The solar wind parameters considered are the orientation of the interplanetary magnetic field, IMF, (B_x, B_y, B_z), and the solar wind velocity, (V_x, V_y, V_z). The results in the case of AE, PCP and B_z are displayed **Figure 5** and **Figure 6**. The superposed epoch analysis of B_x, B_y and V_x, V_y, V_z shows no time variation.

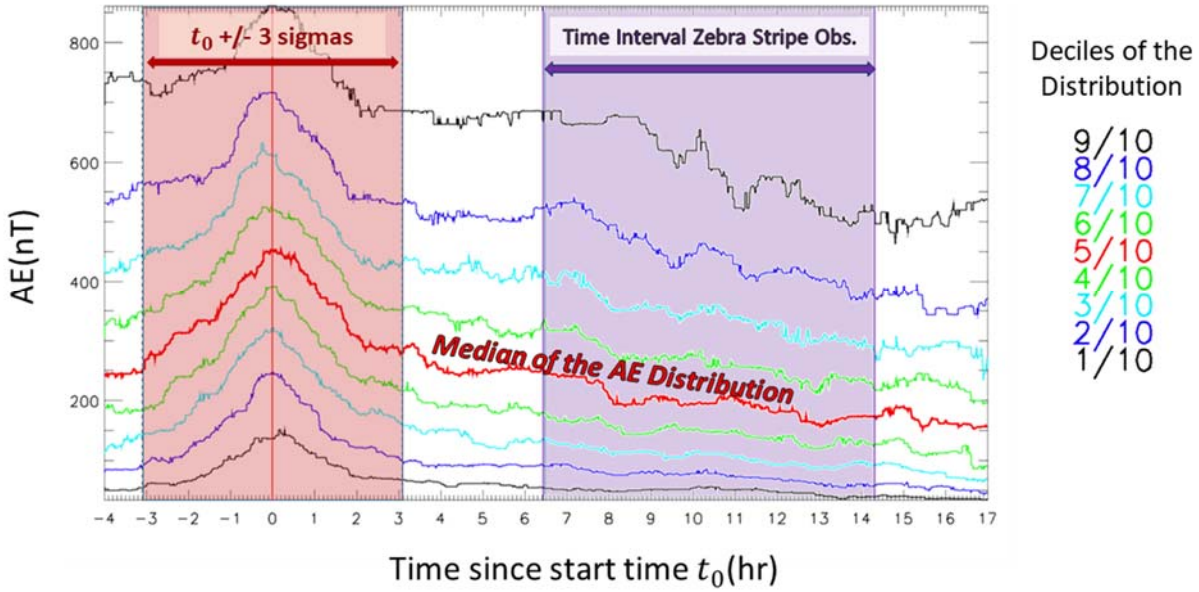

405

406 **Figure 5.** Superposed epoch analysis for the time evolution of the AE index. The time interval
407 starts a few hours before zebra stripe generation. It ends a few hours after zebra stripe
408 disappearance. The start time $t_o = 0$ is indicated by a vertical red line, and the typical margin of
409 error around t_o is depicted by a red rectangle. The typical time interval during which zebra stripes
410 are observed is depicted by a purple rectangle. The average time evolution of the AE index is
411 represented by a thick red line.

412

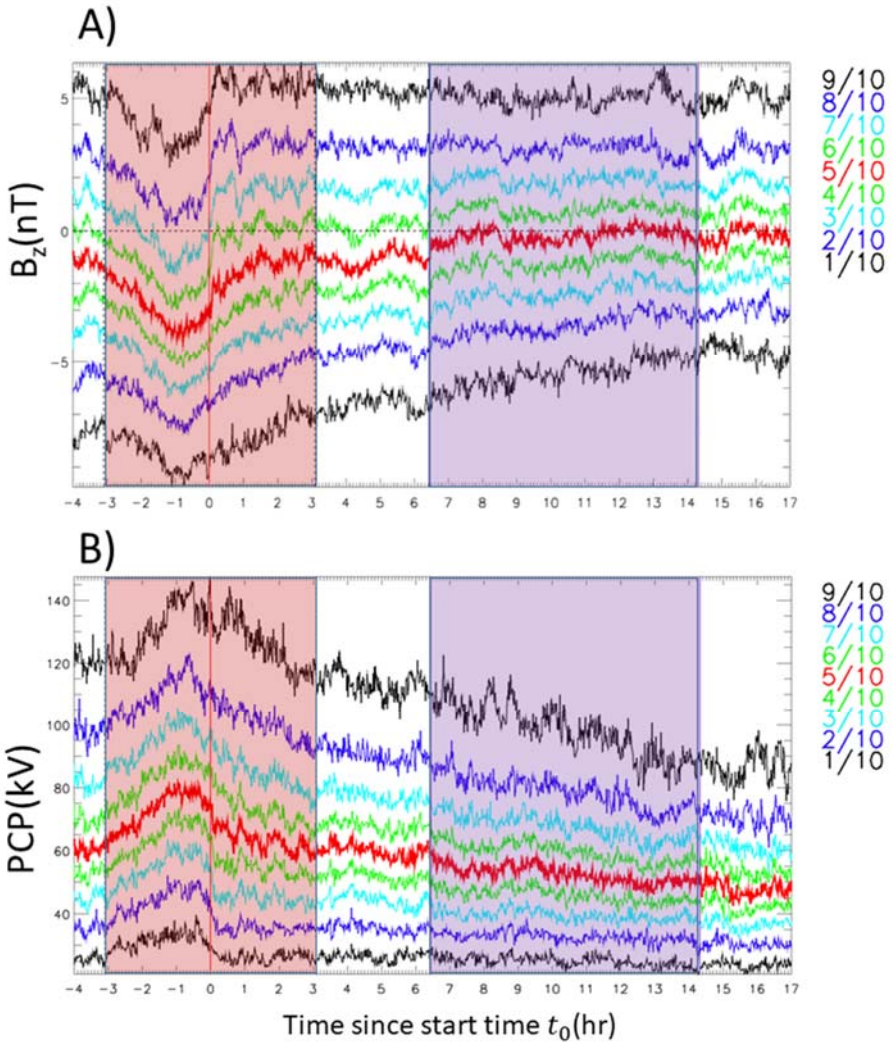

413

414 **Figure 6**. Similar to **Figure 5**, but for the time evolutions of A) the north-south component of the
415 IMF, B_z, and B) the polar cap potential, PCP.

416

417 The time evolution of the magnetic indices around start time is indicative of substorm onset
418 (**Figures 5-6**): The AE index increases (reaching average values greater than 400 nT), the
419 interplanetary magnetic field becomes southward (reaching average values below -3nT), and the
420 polar cap potential increases (reaching average values greater than 75kV). Because the disturbance
421 lasts only a few hours on average, they have subsided by the time the zebra stripes become
422 observable. That is why zebra stripes have been reported during both geomagnetically active and
423 geomagnetically quiet times (e.g., Ukhorskiy et al., 2014).

We have also studied how the magnitude of the zebra stripe pattern varies with the peak magnitude of magnetic activity around start time, t_o. To do so, we compute the extrema reached by the different magnetic indices around start times (+/- 3 sigmas), and we attribute an average stripe magnitude to every event. The average magnitude is equal to the average of the absolute values of the ratios between the flux and the smoothed flux at all the identified extrema. The results, displayed **Figure 7**, show a positive correlation between the magnitude of the zebra stripe pattern and the magnitude of the substorm (as quantified by the maximum in the AE index, the minimum in B_z, or the maximum in PCP around start time). Given that 370 samples were used to compute the correlation coefficients, we conclude that the correlation is statistically significant ($p < 0.01$).

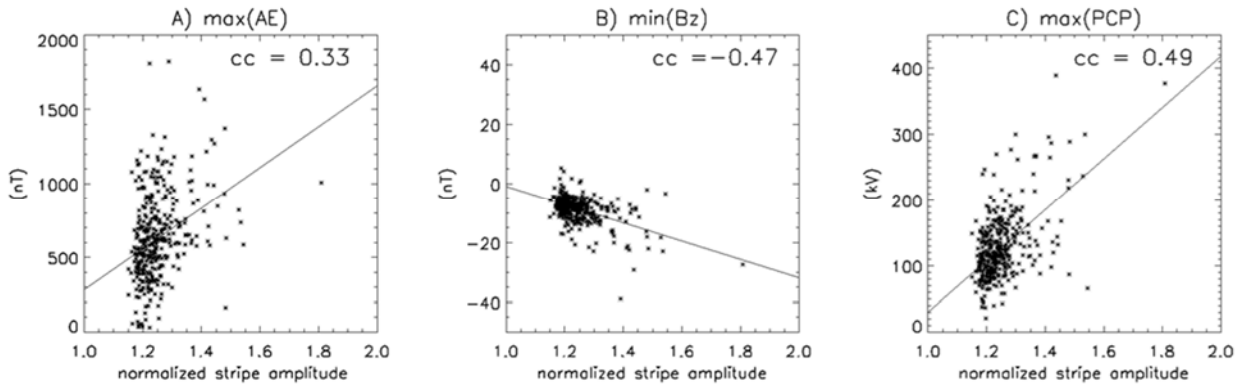

Figure 7. Testing the correlation between the magnitude of different magnetic indices during the start time interval and the magnitude of the resulting stripes. The Pearson correlation coefficients between the average normalized amplitude of the stripes and A) the maximum of AE, B) the minimum of B_z, and C) the maximum of PCP are displayed in the top right corner of every panel. The time interval for the determination of the extrema is $+/-3$ hours around start time t_o. Linear interpolations of the different data sets are also displayed to guide the eye.

These results confirm and refine previous findings by Liu et al. (2016), who obtained a positive correlation between the amplitude of the stripes and the maximum in Kp index over the 12-hr interval preceding observation. The **Figure 7** suggests that the magnitude of the substorm

447 occurring a few hours to half day prior to observations somewhat controls the magnitude of the
448 zebra stripe pattern.
449
450 **3.3. Start Time Azimuthal Locations for the Zebra Stripe Peaks and Valleys**
451
452 Do the peaks (and valleys) originate from some preferred azimuthal locations or can they be
453 generated at any local time during substorm onset? To answer this question, we compute the start
454 time angular location $\varphi(t_0)$ associated with every peak and valley (Ω_i), time and place of
455 measurement $(t, \varphi(t))$, and event start time, t_0, applying the **equation (7)**. We store the set of
456 resulting azimuthal locations (MLT) in a histogram with a 2-hr LT bin size, which we then
457 normalize by the total number of data points in the sample. The resulting graph provides the
458 relative frequency distribution of the initial azimuthal locations. If the peaks and valleys were
459 generated anywhere, without any preferred azimuthal location, the resulting relative frequency
460 distributions would be flat and equal to 1/12~8.3%. In practice, the frequency distribution
461 functions for the peaks and valleys present variations with local time (**Figure 8**).
462

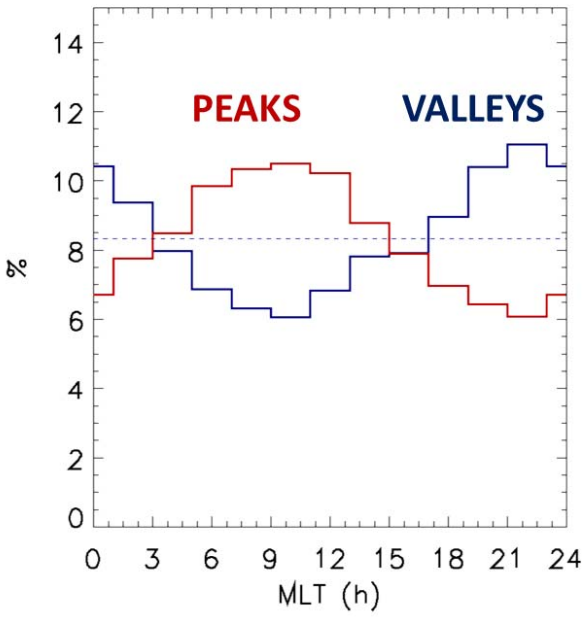

463 **Figure 8.** Relative frequency distribution of the initial azimuthal location, $\varphi(t_0)$, (in red) for the
464 data points corresponding to a peak in the zebra stripe pattern and (in blue) for the data points
465 corresponding to a valley in the zebra stripe pattern. That the two functions vary with magnetic

local time, MLT, indicates that the peaks and valleys are created at preferred azimuthal locations: in the morning sector for the peaks, and in the premidnight sector for the valleys.

The peaks in the zebra stripe patterns are preferentially created in the morning sector, around 9 MLT. On the other hand, the valleys in the zebra stripe patterns are preferentially created in the premidnight sector, around 22 LT. Assuming conservation of the phase space density, a variation of the observed flux j can be reformulated in terms of radial motion ΔL. For instance, in the equatorial case (e.g., Selesnick et al., 2016):

$$\frac{\Delta j}{j} = -\frac{3\Delta L}{L} \tag{8}$$

where L corresponds to the normalized equatorial radial distance. Thus, **Figure 8** suggests that a population of electrons located in the morning sector drifted inward at start time, t_0 ($\Delta L < 0$, thus $\Delta j > 0$), while a population of electrons located in the premidnight sector drifted outward at start time, t_0 ($\Delta L > 0$, thus $\Delta j < 0$). In the inner belt, the magnetic field does not vary much and disturbances in trapped particle drift motion originate mainly from disturbances in the electric drift (e.g., Selesnick et al., 2016). As a result, the **Figure 8** is suggestive of an average scenario in which the zebra stripes are generated by a large-scale electric field appearing during start times, oriented such as to drive a large-scale morning-to-premidnight radial motion of the trapped inner belt particles. Combined with previous findings (**Fig.5-7**), namely, that the start times usually correspond to substorm onset times, and that the amplitude of the stripes is somewhat controlled by the substorm magnitude, experimental evidence suggests that the zebra stripes are most likely generated by the direct penetration of magnetospheric convection in the plasmasphere during substorm onset. In the following **Section 3.4,** we present electric field observations that further validate the proposed scenario.

3.4. Electric Field Perturbations During Zebra Stripe Generation

Under quasi-steady conditions, the plasmasphere is expected to be shielded from the high-latitude electric fields generated by the interaction between the magnetosphere and the interplanetary

495 medium. Undershielding occurs when a rapid increase of magnetospheric convection generates
496 prompt penetration electric fields and currents that extend directly down to midlatitudes and the
497 equator. The disturbances are usually short-lived, with lifetimes from a few minutes to a few hours
498 (e.g. Fejer et al., 2017; Maruyama, 2020). Such a short lifetime makes the prompt penetration
499 electric fields more difficult to detect than the subcorotation related to the ionospheric disturbance
500 dynamo, the latter lasting from several hours to a couple of days (e.g., Blanc & Richmond, 1980;
501 Lejosne & Mozer, 2018). By analyzing as many events as possible, we increase the chances of a
502 spacecraft being at the right place and time to detect prompt penetration electric fields.
503
504 We compile all the electric field measurements sampled when a spacecraft was located between L
505 = 1.5 and L = 2.5 during one of the 370 start time intervals (t_o $+/-3$ hours). Because the
506 undershielding process is associated with times when the IMF becomes southward, we restrict the
507 database to the points measured when the IMF-B_z is negative. The resulting dataset of electric field
508 measurements is then analyzed as a function of local time. There are 4000 data points on average
509 per 2-hr local time bin (min: 2700 points per bin; max: 6500 points per bin), and the data covers
510 70 different events on average per 2-hr local time bin (min: 58 events per bin; max: 89 events per
511 bin). Thus, although the spacecraft were not always at the right place and the right time (i.e. in the
512 inner belt, between L = 1.5 and L = 2.5, during the 370 start time intervals), there is still enough
513 data points to statistically determine the electric field conditions associated with zebra stripe
514 generation.
515
516 A radial transport across L shells requires a perturbation in the electric field. Thus, the objective
517 is to analyze perturbations in the typical values of the electric field, rather than the total electric
518 field itself. To study the response of experimental electric field measurements to magnetic activity,
519 we follow the common practice that consists of detrending the electric fields (e.g. Fejer &
520 Scherliess, 1997; Huang, 2019). To detrend the electric fields, we first compute a typical value at
521 each sampling point by determining the median value of all electric field measurements at the same
522 location over the three days prior to measurement. The electric field perturbation is then defined
523 by subtracting the typical value to the instantaneous measurement.

For every 2-hr local time bin, the cumulative distributions are examined and the distribution deciles are stored for both components of the electric field perturbations. The results are displayed **Figure 9**.

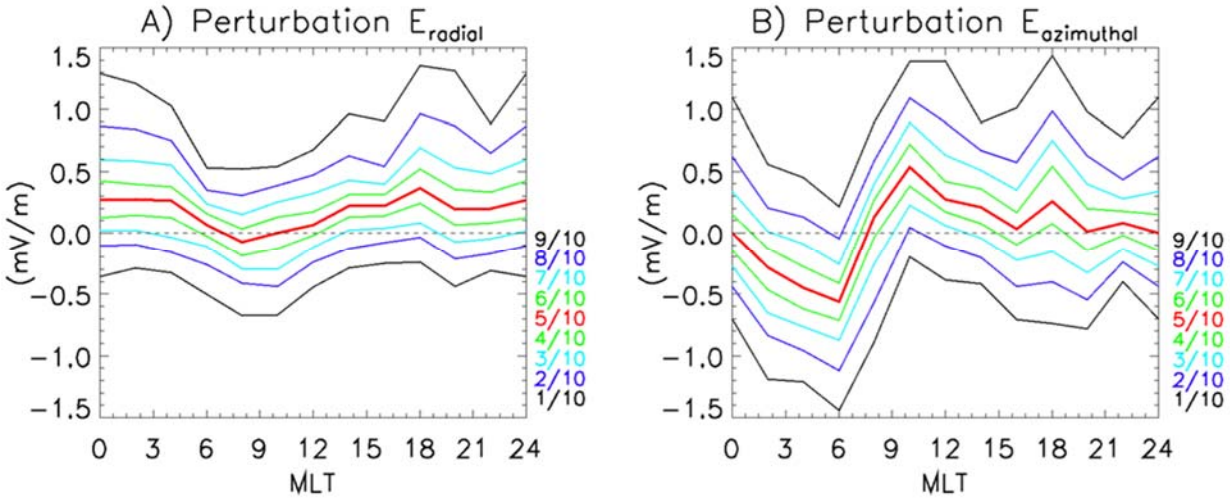

Figure 9. Superposed epoch analysis for the A) radial and B) azimuthal components of the electric field perturbation during the start time intervals associated with zebra stripe generation (when $B_z < 0$ and the spacecraft location L is between 1.5 and 2.5). The average value of the electric field perturbation is represented by a red line. When mapped to the ionosphere, the radial component of the electric field is poleward, and the azimuthal component is zonal.

On average, the radial component of the electric field perturbation is positive. This indicates a plasmaspheric subcorotation during the zebra stripe generation events. The azimuthal component of the electric field perturbation is usually negative on the postmidnight-dawn sector, and positive in the dayside sector. It is worth mentioning that the orientation of the penetration electric field is different from what one would obtain by simply extrapolating a dawn-to-dusk convection electric field, because of spatial variations in ionospheric conductivities (e.g. Senior & Blanc, 1984).

Since previous results (including **Figure 7**) suggest that the amplitude of the electric field perturbation depends on magnetic activity, we test this assumption by computing the Pearson correlation coefficients between the electric field perturbation at different LT bins, and magnetic activity. Both electric field perturbation components are considered, and different magnetic indices are tested (namely, AE, $-B_z$, and PCP). The results are displayed **Figure 10**.

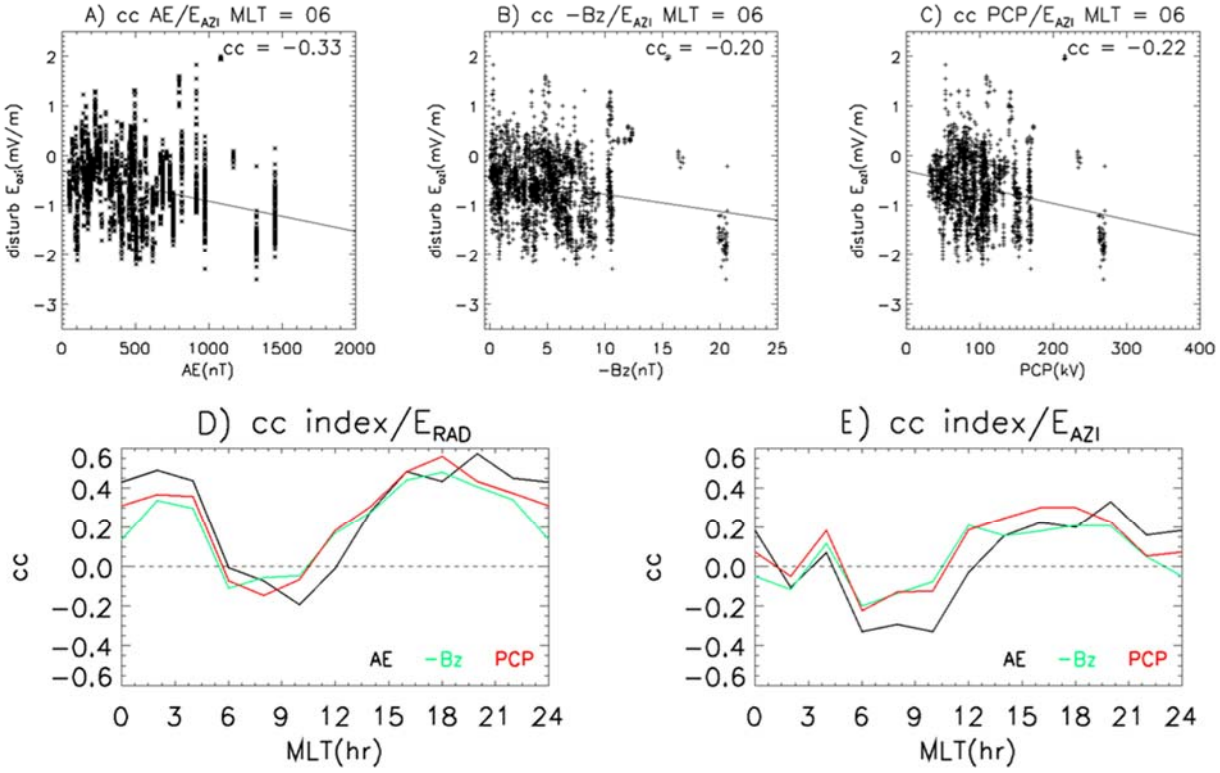

Figure 10. Pearson correlation coefficients (cc) between (1) the azimuthal component of the electric field perturbation measured during zebra stripe generation events, for $LT = 6 +/- 1hr$ and $L \in [1.5,2.5]$, and (2) A) the auroral electrojet AE, B) the south-north component of the IMF: $-B_z$ and C) the polar cap potential, PCP. The bottom panels present a compilation of the different Pearson correlation coefficients as a function of local time, obtained D) for the radial component of the electric field perturbation and different magnetic activity indices (AE in black, $-B_z$ in green and PCP in red), and E) for the azimuthal component of the electric field perturbation and the same magnetic activity indices.

The radial component of the electric field perturbation increases as magnetic activity increases. Thus, the plasmaspheric subcorotation increases as magnetic activity increases. The increase is uniform in LT, everywhere except in the morning sector (6-12LT). For the azimuthal component of the electric field, the field decreases as magnetic activity increases around 6-9LT. Thus, there is inward motion around 6-9LT as magnetic activity increases. Similarly, the azimuthal component of the electric field increases as the magnetic activity increases in the dusk sector, leading to

563 outward radial motion around 18-21LT. These findings are consistent with the results displayed
564 **Figure 8**. It is the first time that the signature of the prompt penetration electric fields is observed
565 in near-equatorial electric field measurements.
566
567
568 **4. Summary and Discussion**
569
570 We designed an algorithm to detect and analyze the zebra stripes observed by the RBSPICE
571 instruments onboard the Van Allen Probes. Approximately 12,000 inner belt passes between
572 January 1, 2013 and December 31, 2015 were examined to determine 370 times associated with
573 zebra stripe pattern generation. The events selected are such that zebra stripes are strong and clean
574 enough to be detected during at least two Van Allen Probes passes in the inner belt. Statistical
575 analyses of these 370 events revealed that:
576 (1) the zebra stripes have a lifetime of the order of half a day;
577 (2) the zebra stripes are usually generated during substorm onset;
578 (3) the magnitude of substorm onset is somewhat correlated to the magnitude of the zebra stripe
579 pattern that is observed a few hours later;
580 (4) the peaks in the zebra stripe pattern are preferentially created in the morning sector, around 9
581 MLT, while the valleys in the zebra stripe pattern are preferentially created in the premidnight
582 sector, around 22 LT;
583 (5) a perturbation in the electric field appears during zebra stripe generation events: it leads to
584 inward radial motion around 6-9LT and outward radial motion around 18-21LT.
585
586 Thus, experimental evidence is suggestive of a scenario in which the prompt penetration electric
587 field associated with substorm onset leads to a large-scale perturbation of the trapped particle drift
588 motion. The inward motion of the population located in the dawn-morning sector at onset generates
589 the peaks appearing in the trapped particle spectrograms. Similarly, the outward motion of the
590 population located in the dusk-premidnight sector at onset generates the valleys appearing in the
591 trapped particle spectrograms. In that context, the zebra stripes are nothing more than inner belt
592 drift echoes due to asymmetric electric field variations that are sudden on the time scale of a drift
593 period (e.g. Brewer et al., 1969). Additional work is nonetheless necessary in order to test whether

the amplitude and duration of the prompt penetration electric fields are sufficient to account for the observed amplitudes of zebra stripe patterns.

Large-scale electric fields in the plasmasphere evolve on a variety of timescales that are difficult to disentangle. This study illustrates how the analysis of trapped particle dynamics in the inner belt provides information on the timescales associated with the different electric field components. Indeed, any asymmetric electric field variation that is sudden on the time scale of a drift period drives irreversible radial transport. This leads to the apparition of drift echoes, whose amplitudes relate to the strength of the electric field variation. On the other hand, slow electric field variations lead to reversible effects. This drives electric drift shell splitting, whose magnitude relates to the strength of the electric field asymmetry (e.g. Selesnick et al., 2016). In that context, the analysis of variations in the spectrograms of energetic particles trapped in the Earth's inner belt constitutes another tool to examine the dynamics of the middle and low latitude (i.e., plasmaspheric) electric fields.

Acknowledgements

The work was performed under JHU/APL Contract No. 922613 (RBSP-EFW) and NASA Grant Award 80NSSC18K1223. We acknowledge the use of NASA/GSFC's Space Physics Data Facility's OMNIWeb (https://omniweb.gsfc.nasa.gov/) service and OMNI data. The data used in this paper are in public access in the RBSP/EFW database (http://www.space.umn.edu/rbspefw-data/), in the RBSPICE database (http://rbspice.ftecs.com/Data.html)
The RBSPICE instrument was supported by JHU/APL Subcontract No. 937836 to the New Jersey Institute of Technology under NASA Prime Contract No. NAS5-01072.
The Fortran Library International Radiation Belt Environment Modeling (IRBEM-LIB) can be downloaded at http://sourceforge.net/projects/irbem/

621 **References**

622

623 Boscher, D., S. Bourdarie, P. O'Brien, and T. Guild (2012), IRBEM Library, Version 4.4.0.

624

625 Boyle, C. B., Reiff, P. H., and Hairston, M. R. (1997), Empirical polar cap potentials, J. Geophys.
626 Res., 102(A1), 111– 125, doi:10.1029/96JA01742.

627

628 Brewer, H. R., Schulz, M., and Eviatar, A. (1969), Origin of drift-periodic echoes in outer-zone
629 electron flux, J. Geophys. Res., 74(1), 159– 167, doi:10.1029/JA074i001p00159.

630

631 Cladis, J. B. (1966), Resonance acceleration of particles in the inner radiation belt, in Radiation
632 Trapped in the Earth's Magnetic Field, edited by B. M. McCormac, pp. 112–115, D. Reidel,
633 Hingham, Mass.

634

635 Datlowe, D. W., W. L. Imhof, E. E. Gaines, and H. D. Voss (1985), Multiple peaks in the spectrum
636 of inner belt electrons, J. Geophys. Res., 90, 8333–8342, doi:10.1029/JA090iA09p08333.

637

638 Duda, R.O.; Hart, P. E. (January 1972). "Use of the Hough Transformation to Detect Lines and
639 Curves in Pictures". Comm. ACM. 15: 11–15. doi:10.1145/361237.361242

640

641 Fejer, B. G., Blanc, M., & Richmond, A. D. (2017). Post-storm middle and low-latitude
642 ionospheric electric field effects. Space Science Reviews, 206(1-4), 407–429.
643 https://doi.org/10.1007/s11214-016-0320-x

644

645 Fejer, B. G., and Scherliess, L. (1997), Empirical models of storm time equatorial zonal electric
646 fields, J. Geophys. Res., 102(A11), 24047– 24056, doi:10.1029/97JA02164.

647

648 Huang, C.-S. (2019). Long-lasting penetration electric fields during geomagnetic storms:
649 Observations and mechanisms. Journal of Geophysical Research: Space Physics, 124. https://
650 doi.org/10.1029/2019JA026793

651

652 Kletzing, C.A. et al. (2013). The Electric and Magnetic Field Instrument Suite and Integrated
653 Science (EMFISIS) on RBSP, Space Sci. Rev., 179, 127-181. doi: 10.1007/s11214-013-993-306
654 6
655
656 Imhof, W. L. and Smith, R. V. (1965), Observation of Nearly Monoenergetic High-Energy
657 Electrons in the Inner Radiation Belt, Phys. Rev. Lett., 14, 22, 885—887,
658 doi:10.1103/PhysRevLett.14.885
659
660 Imhof, W. L., E. E. Gaines, and J. B. Reagan (1981a), High-resolution spectral features observed
661 in the inner radiation belt trapped electron population, J. Geophys. Res., 86, 2341–2347,
662 doi:10.1029/JA086iA04p02341
663
664 Imhof, W. L., E. E. Gaines, and J. B. Reagan (1981b), Observations of multiple narrow energy
665 peaks in electrons precipitating from the inner radiation belt and the implication for wave particle
666 interactions, J. Geophys. Res., 86, 1591–1595, doi:10.1029/JA086iA03p01591.
667
668 Lejosne, S., and F.S. Mozer (2016a), Van Allen Probe measurements of the electric drift E×B/B^2
669 at Arecibo's L=1.4 field line coordinate, Geophys. Res. Lett., 43, 6768-6774, doi:
670 10.1002/2016GL069875.
671
672 Lejosne, S., and Mozer, F.S. (2016b). Typical values of the electric drift E×B/B^2 in the inner
673 radiation belt and slot region as determined from Van Allen Probe measurements, J. Geophys.
674 Space Physics, 121. doi: 10.1002/2016JA023613
675
676 Lejosne, S., and Roederer, J. G. (2016), The "zebra stripes": An effect of F region zonal plasma
677 drifts on the longitudinal distribution of radiation belt particles, J. Geophys. Res. Space Physics,
678 121, 507– 518, doi:10.1002/2015JA021925.
679
680 Lejosne, S., S. Maus, and F. S. Mozer (2017). Model-observation comparison for the geographic
681 variability of the plasma electric drift in the Earth's innermost magnetosphere, Geophys. Res. Lett.,
682 44, 7634–7642. https://doi.org/10.1002/2017GL074862

Lejosne, S., and F.S. Mozer (2018). Magnetic activity dependence of the electric drift below L=3, Geophys. Res. Lett., doi: 10.1029/2018GL077873.

Lejosne, S., and Mozer, F.S. (2019). Shorting factor in-flight calibration for the Van Allen Probes DC electric field measurements in the Earth's plasmasphere. Earth and Space Science, 6, 646– 654. https://doi.org/10.1029/2018EA000550.

Liu, Y., Zong, Q.-G., Zhou, X.-Z., Foster, J. C., and Rankin, R. (2016), Structure and evolution of electron "zebra stripes" in the inner radiation belt, J. Geophys. Res. Space Physics, 121, 4145–4157, doi:10.1002/2015JA022077.

Maruyama, N. (2020), Chapter 9 - Storms and substorms—The new whole system approach and future challenges, in T*he Dynamical Ionosphere*, Elsevier, https://doi.org/10.1016/B978-0-12-814782-5.00009-1.

Mitchell, D.G., Lanzerotti, L.J., Kim, C.K. et al. Radiation Belt Storm Probes Ion Composition Experiment (RBSPICE). Space Sci Rev (2013) 179: 263. https://doi.org/10.1007/s11214-013-9965-x

Mozer, F. S. (2016), DC and low-frequency double probe electric field measurements in space, J. Geophys. Res. Space Physics, 121, 10,942– 10,953, doi:10.1002/2016JA022952.

Pinto, O. Jr., Pinto, I. R. C. A., Gonzalez, W. D., & Gonzalez, A. L. C. (1991). About the origin of peaks in the spectrum of inner belt electrons. Journal of Geophysical Research, 96(A2), 1857–1860. https://doi.org/10.1029/90JA02383

Sauvaud, J.-A., M. Walt, D. Delcourt, C. Benoist, E. Penou, Y. Chen, and C. T. Russell (2013), Inner radiation belt particle acceleration and energy structuring by drift resonance with ULF waves during geomagnetic storms, J. Geophys. Res. Space Physics, 118, 1723–1736, doi:10.1002/jgra.50125

Schulz, M. and Lanzerotti, L.J. (1974), Particle Diffusion in the Radiation Belts. Springer-Verlag Berlin Heidelberg. https://doi.org/10.1007/978-3-642-65675-0

Selesnick, R. S., Y.-J. Su, and J.B. Blake (2016), Control of the innermost electron radiation belt by large-scale electric fields, J. Geophys. Res. Space Physics, 121, doi:10.1002/2016JA022973.

Senior, C., and Blanc, M. (1984), On the control of magnetospheric convection by the spatial distribution of ionospheric conductivities, J. Geophys. Res., 89(A1), 261– 284, doi:10.1029/JA089iA01p00261.

Su, Y.-J., Selesnick, R. S., and Blake, J. B. (2016), Formation of the inner electron radiation belt by enhanced large-scale electric fields, J. Geophys. Res. Space Physics, 121, 8508– 8522, doi:10.1002/2016JA022881.

Sun, Y., Hao, Y., Zong, Q., Roussos, E., Liu, Y., & Yuan, C. (2019). Zebra stripes at Earth and Saturn and the influence of energetic electron convection. AGU Fall Meeting. San Francisco, CA, USA. 2019-12-09 - 2019-12-13.

Ukhorskiy, A. Y., M. I. Sitnov, D. G. Mitchell, K. Takahashi, L. J. Lanzerotti, and B. H. Mauk (2014), Rotationally driven 'zebra stripes' in Earth's inner radiation belt, Nature, 507, 338–340, doi:10.1038/nature13046.

Wygant et al. (2013), The Electric Field and Wave Instruments on the Radiation Belt Storm Probes Mission, Space Sci. Rev., 179, 183-220, doi:10.1007/s11214-013-0013-7